Artemisiae Scopariae Herba (Yinchen) suppresses ferroptosis in mice with osteoporosis via the Nrf2/Slc7a11/Gpx4 pathway

PEI LI*, XINYU WAN*, WENJIE LI, DING CHENG, YING YANG, YUHAN WANG, RUYUAN ZHU, YANJING CHEN, HAIXIA LIU and ZHIGUO ZHANG

Institute of Basic Theory for Chinese Medicine, China Academy of Chinese Medical Sciences, Beijing 100700, P.R. China

Received May 13, 2025; Accepted November 19, 2025

DOI: 10.3892/mmr.2026.13793

Abstract. With the aging of the population, the incidence of postmenopausal osteoporosis (PMOP) is increasing. Extracts from Artemisiae Scopariae Herba, also known as Yinchen (YC), promote osteogenic differentiation and bone formation; however, the specific mechanism is unclear. The present study aimed to investigate the effects and mechanism of YC on PMOP. Ultra-performance liquid chromatography-tandem mass spectrometry was used to determine the potential predominant components of YC, and an ovariectomized (OVX) mouse model was established to evaluate the effects of YC on PMOP and its potential mechanisms. Initially, the therapeutic effect of YC on PMOP was assessed by micro-CT bone analysis, pathological observation and ELISA detection. Combined with serum ELISA, reverse transcription-quantitative PCR and immunohistochemical staining, the potential key anti-PMOP pathway of YC was explored. A total of 2,072 compounds were identified in YC. The main active components of YC included chlorogenic acid, ferulic acid and caffeic acid. Experimental studies provided evidence that YC may improve bone loss and bone microstructure deterioration caused by ovariectomy. YC treatment also upregulated serum estrogen levels, and the expression of osteoprotegerin, runt-related transcription factor 2 and glutathione peroxidase 4 (Gpx4) in bone tissue. Ovariectomy led to abnormal iron metabolism and increase the accumulation of lipid peroxides. YC reduced liver iron deposition, restored glutathione levels, and downregulated serum tartrate-resistant acid phosphatase, osteocalcin, ferritin and hepcidin levels in mice. In addition, YC reversed the decreased expression of nuclear factor erythroid 2-related factor 2 (Nrf2), solute carrier family 7 member 11 (Slc7a11) and Gpx4 in the bone tissues of OVX mice. In conclusion, the present study suggested the effectiveness of YC in potentially reducing ovariectomy-induced osteoporosis in mice. YC promoted bone formation and improved bone microstructure, potentially by inhibiting ferroptosis via activation of the Nrf2/Slc7a11/Gpx4 pathway in OVX mice.

Correspondence to: Professor Haixia Liu or Professor Zhiguo Zhang, Institute of Basic Theory for Chinese Medicine, China Academy of Chinese Medical Sciences, 16 Nanxiaojie, Dongzhimennei, Dongcheng, Beijing 100700, P.R. China
E-mail: lhx8866_7@163.com
E-mail: zzgtcm@163.com

*Contributed equally

Key words: postmenopausal osteoporosis, Artemisiae Scopariae Herba, Yinchen, ferroptosis, nuclear factor erythroid 2-related factor 2/solute carrier family 7 member 11/glutathione peroxidase 4 pathway, bone formation

Introduction

Estrogen deficiency-induced osteoporosis is a bone metabolic disease characterized by changes in bone density and microstructure, resulting in increased bone fragility and a higher risk of fracture. After menopause, patients lose ~50% of trabecular bone mass and 30% of cortical bone mass compared with those at 20-30 years of age (1). Postmenopausal osteoporosis (PMOP) is directly related to an increased risk of bone fracture. A European Union study showed that a 50-year-old female patient has a 46% chance of developing an osteoporotic fracture in their lifetime (2). Currently, the commonly used therapeutic drugs in clinics for PMOP include hormone replacement therapy, bisphosphonate, parathyroid hormone and selective estrogen receptor modulators. Hormone replacement therapy is the most effective treatment, but is associated with risks such as breast cancer, uterine bleeding and cardiovascular disease (3).

YC is the dry aboveground part of *Artemisia scoparia* Waldst. et Kit. or *Artemisia capillaris* Thunb. YC extract alleviates bone loss through a dual mechanism: Enhancing osteoblast-mediated mineralization and suppressing osteoclast differentiation (4). Using mass spectrometric analysis and activity screening, subsequent studies have further identified specific bioactive constituents responsible for inhibiting osteoclast formation and bone resorption, primarily via attenuation of acidification processes. These findings indicate the potential of YC as a natural candidate for the treatment of osteoporosis (4,5). The main components of YC include coumarin, flavonoids, organic acids, volatile oil and terpenoids, which have anti-inflammatory, antioxidative, antibacterial, cytoprotective and anti-osteoporotic effects. Chlorogenic acid, artemisinolide, hyperoside and scopoletin have been reported to be the most active ingredients in the extract (6-11).

Chlorogenic acid can promote bone marrow stromal cell (BMSC) proliferation and osteogenic differentiation through the Shp2 pathway (12). In addition, chlorogenic acid upregulates the neuronatin gene in ovariectomized (OVX) mice, activates the MAPK signaling pathway and promotes the osteogenic differentiation of BMSCs (13). It can also activate the nuclear factor erythroid 2-related factor 2 (Nrf2)/heme oxygenase 1 (HO-1) pathway, inhibit the excessive production of reactive oxygen species (ROS) and reduce oxidative stress levels (14). Chlorogenic acid has also been shown to downregulate the receptor activator of NF-κB ligand (RANKL)-induced phosphorylation of p38 and ERK in bone marrow macrophages, and to inhibit the expression of nuclear factor of activated T-cells, cytoplasmic 1, thereby inhibiting osteoclast differentiation and bone resorption (15,16). Hyperoside can promote the proliferation and osteogenic differentiation of BMSCs and improve the bone microstructure of OVX mice by enhancing microRNA-19a-5p and downregulating IL-17A (16-18). Furthermore, YC can downregulate the expression of NADPH oxidase 1 and inhibit RANKL-induced osteoclast differentiation, thereby inhibiting bone loss (17). Scopoletin can inhibit osteoclast differentiation by scavenging ROS (19).

Cell death consists of programmed cell death and non-programmed cell death. In 2012, Dixon *et al* (20) proposed ferroptosis as a new mode of cell death that is different from other methods of programmed cell death. When cells are subjected to excess stimulation or the antioxidant system is defective, lipid peroxides will gradually accumulate and eventually trigger ferroptosis. Glutathione peroxidase 4 (Gpx4) was the first core inhibitor of ferroptosis identified, and other Gpx4-independent pathways or factors that inhibit ferroptosis have since been found, including the system xc^-/Gpx4, ferroptosis suppressor protein 1/NAD(P)H/coenzyme Q10 and GTP cyclohydrolase 1/Tetrahydrobiopterin/dihydrofolate reductase axes (21-23). System xc-is a cystine/glutamate antiporter composed of the solute carrier family 7 member 11 (Slc7a11) and Slc3a2 subunits, which is crucial for cellular glutathione synthesis and antioxidant defense. Dysfunction of Slc7a11 can impair cystine uptake, leading to glutathione depletion and heightened susceptibility to ferroptosis (24). Lipid peroxidation is an important factor for ROS-induced oxidative stress in bone tissue. Gpx4-knockout mice show a notable reduction in bone mineral density (BMD) and ovariectomy can aggravate osteoporosis in Gpx4-knockout mice (25). Nrf2 is also important for regulating ferroptosis in osteocytes. Knockdown of Nrf2 in osteocytes can induce ferroptosis and activation of Nrf2 can inhibit RANKL expression (26).

YC is a potential drug for preventing osteoporosis; ferroptosis may be a potential target for the treatment of osteoporosis; and the Nrf2/Slc7a11/Gpx4 pathway is an important pathway in regulating ferroptosis. However, the regulatory effects of YC on ferroptosis in osteoporosis remain ambiguous. Therefore, the present study aimed to investigate the regulatory effect of YC on PMOP from the perspective of ferroptosis and to further explore the effect of YC on the Nrf2/Slc7a11/Gpx4 ferroptosis regulatory pathway.

Materials and methods

Experimental drugs. YC (TongRenTang Chinese Medicine) was mixed with distilled water in a magnetic stirrer for 2 h at room temperature and then crushed using a juicer. The juice was then filtered and concentrated in a rotary evaporator to obtain 1 and 0.5 g/ml of solution, which was stored at -20˚C for later use. Estradiol valerate acid tablets (EV) (cat. no. J20130009; Bayer) were ground into powder, dissolved in distilled water a suspension of estradiol was obtained in an ultrasound-assisted manner with a concentration of 0.013 mg/ml.

Experimental animals. The study was conducted in strict accordance with the animal experiment ethics regulations of the Institute of Basic Theory for Chinese Medicine, China Academy of Chinese Medical Sciences and were approved by the Institutional Animal Ethics Committee (approval no. IBTCMCACMS21-2303-04; Beijing, China). A total of 40 specific pathogen-free female C57BL/6 mice (age, 8 weeks; weight, 20±2 g) were obtained from SPF Biotechnology Co., Ltd. [license no. SCXK(Beijing)2021-0010]. The mice were housed under conventional conditions (room temperature 22±1˚C, humidity 50±5%, 12/12-h light/dark cycle) with free access to food and water. They were randomly divided into five groups: i) Sham operation (SHAM) group treated with 10 ml/kg distilled water via oral gavage; ii) OVX model group treated with 10 ml/kg distilled water via oral gavage; iii) EV group treated with 0.13 mg/kg EV for 12 weeks via oral gavage; iv) YC low dose (YCL), treated with 5 g/kg YC water extract via oral gavage for 12 weeks; and v) YC high dose (YCH) group treated with 10 g/kg YC water extract via oral gavage for 12 weeks. Bilateral ovariectomy was performed on mice in the OVX and medication groups. Briefly, the mice were anesthetized by intraperitoneal injection of 1% pentobarbital sodium (50 mg/kg). An incision was made on the dorsal side, cauliflower-like ovarian tissue was ligated, the ovaries were removed and the wound was sutured. In the Sham group, the operation was the same as for the experimental groups but only a small amount of adipose tissue surrounding the ovary was ligated and excised. Drugs were given starting 1 week after surgery, continuing for 12 weeks, with all treatments administered once daily at the same time each day.

After the last administration, the mice were euthanized by an intraperitoneal overdose of pentobarbital sodium (100 mg/kg) and death was confirmed by a cessation of heartbeat and respiration. Blood was collected via cardiac puncture (0.8-1.2 ml per mouse) and allowed to stand at room temperature for 2 h. The uterus was dissected and weighed, and the uterine coefficient was calculated as uterine wet weight (mg)/body weight (g). The liver was removed and fixed in 4% paraformaldehyde (PFA) fixation solution at room temperature for 24 h, whereas the femur was fixed in 4% PFA fixation solution at room temperature for 48 h after removing the muscle from the bone. Subsequently, the fixation solution was replaced with fresh 4% PFA for long-term storage at room temperature. The tibia was preserved at -80˚C. Humane endpoints were defined as follows: Severe weight loss (>20%), inability to access food or water, signs of severe pain or distress, such as hunched posture, lethargy or vocalization, or any other condition that would compromise animal welfare. No animals reached these endpoints during the study.

Ultra-performance liquid chromatography-tandem mass spectrometry (UPLC-MS/MS). The aforementioned prepared

water solution of YC was added to an equal amount of internal standard extract (70% methanol), centrifuged at ~13,800 x g for 3 min at 4˚C and the supernatant was filtered through a 0.22-μm filter membrane to obtain the sample for later use. Analysis was performed on Agilent SB-C18 columns (.8 μm, 2.1 mm x 100.0 mm; Agilent Technologies, Inc.) using an ExionLC AD UPLC system (Sciex). The liquid phase conditions consisted of a mobile phase, in which phase A was ultrapure water with 0.1% formic acid and phase B was acetonitrile with 0.1% formic acid. The elution gradient was as follows: i) 0 min, the proportion of phase B was 5%; ii) 9 min, the proportion of phase B linearly increased to 95% and was maintained for 1 min; and iii) subsequently the proportion of phase B decreased to 5% and was equilibrated at 5% for 14 min. The flow rate was 0.35 ml/min, the column temperature was 40˚C and the injection volume was 2 μl. MS conditions were as follows: Electrospray ionization source temperature, 550˚C; ion spray voltage, 5,500 V (positive ion mode)/-4,500 V (negative ion mode); ion source gas I, gas II and curtain gas were set to 50, 60 and 25 psi, respectively; and the collision-induced ionization parameter was set to high. Scans were performed in multiple reaction monitoring (MRM) mode with the collision gas, nitrogen, set to medium. The de-clustering potential and collision energy of each MRM ion pair were further optimized. A specific set of MRM ion pairs was monitored at each period based on the metabolites eluted within each period. A specific set of MRM transitions was monitored for each period according to the metabolites eluted within this period, based on the optimized precursor ion (Q1) and product ion (Q3) m/z values. Finally, components that have been proven to have anti-osteoporotic activity in existing literature were selected from the 2,072 compounds for further investigation in the present study (5,18,19).

Micro-CT. To evaluate the changes in bone morphology in mice, micro-CT was performed on the femurs of mice using Skyscan1276 (Bruker) with the following scan parameters: 6.5 μm, 70 kV and 200 mA. The lowest point of the lateral growth plate of the femoral knee joint was taken as the baseline and the area with a thickness of 1 mm was set as the 3D reconstruction area of interest. The NRecon software (version 1.7.1.0, Bruker) was used for 3D image reconstruction and the CTAn software (version 1.17.7.2, Bruker) was used to evaluate the BMD (mg/cm^3), bone volume/total volume (BV/TV, %), trabecular number (Tb.N, 1/mm), trabecular separation (Tb.Sp, mm) and structure model index (SMI).

ELISA. Blood was collected following euthanasia by an overdose of pentobarbital sodium (as aforementioned) via cardiac puncture, with 0.8-1.2 ml collected per mouse. Serum was collected by centrifugation at 1,900 x g for 15 min at 4˚C after 2 h at room temperature. in addition, mouse tibias were ground into a powdery form under liquid nitrogen using a grinding mill. PBS was added to the powdered tibia samples, and homogenized using a low-temperature grinder. Subsequently, the homogenate was centrifuged at 1,900 x g for 15 min at 4˚C and the supernatant was collected for analysis. The levels of malondialdehyde (MDA), 4-hydroxynonenal (4-HNE), and glutathione (GSH) in the mouse tibia and serum, as well as estradiol (E2), tartrate-resistant acid phosphatase (TRAP), and osteocalcin (OCN) in serum alone, were detected using commercial ELISA kits strictly according to the manufacturers' protocols. The specific kits employed were as follows: Mouse MDA ELISA Kit (cat. no. F9264-A; Shanghai Kexing Trading Co., Ltd.), Mouse 4-HNE ELISA Kit (cat. no. F9213-A; Shanghai Kexing Trading Co., Ltd.), Mouse GSH ELISA Kit (cat. no. F2658-A; Shanghai Kexing Trading Co., Ltd.), and Mouse E2 ELISA Kit (cat. no. MB-3302A; Jiangsu Meibiao Biotechnology Co., Ltd.). The absorbance was recorded at 450 nm. A standard curve was generated from the absorbance values of the standard wells, which allowed for the calculation of sample concentration.

Hematoxylin and eosin (H&E) staining. H&E staining was performed on 5-μm paraffin-embedded mouse femur sections to distinguish bone trabeculae from bone marrow. The femurs were dehydrated through a graded ethanol series, cleared in xylene, and embedded in paraffin prior to sectioning. The sections were baked at 67˚C for 2 h, deparaffinized in xylene I and II (10 min each) and rehydrated through a graded ethanol series (100, 95 and 75%; 3 min each). Subsequently, the sections were stained with hematoxylin at room temperature for 3 min, rinsed with tap water, differentiated, blued and washed again. After dehydration in 75 and 95% ethanol (5 min each), eosin staining was carried out at room temperature for 5 min, followed by rinsing with distilled water. Sections were further dehydrated in absolute ethanol (three changes, 5 min each), cleared in xylene and mounted with neutral resin. Finally, images were acquired using a slide scanner.

Masson's trichrome. Masson's staining can stain collagen fibers blue, reflecting the maturity of bone tissue. Femoral specimens of mice were fixed and decalcified, before being embedded as aforementioned. The slices were baked at 67˚C for 2 h, deparaffinized, and rehydrated. The slices were stained sequentially at room temperature using Weigert's iron hematoxylin for 5 min, ponceau magenta for 5 min and aniline blue for 1 min. Following dehydration, the slices were sealed with neutral resin. Finally, the images were acquired by scanning the slices using a slide scanner.

Prussian blue dyeing. Under acidic conditions, potassium ferrocyanide can react with iron trivalent to form a blue compound, Prussian blue, to detect liver iron ion levels. The liver tissue was dehydrated with a gradient alcohol series and permeabilized by xylene after fixation but before embedding. The paraffin-embedded liver was then cut into 5-μm sections and placed on a slide to dry. Following dewaxing as aforementioned, the Prussian blue stain was prepared according to the manufacturer's instructions (Solarbio, G1422) and added at room temperature for 20 min, before sections were washed with distilled water for 5 min. Sections were stained with nuclear solid red at room temperature for 8 min and rinsed for 3 sec. After dehydration, the sections were sealed with neutral resin and the images were scanned by a slide scanner.

Immunohistochemistry staining. Mouse femur specimens were fixed, decalcified, embedded and sectioned as aforementioned. Sections were deparaffinized, antigen retrieval was performed using EDTA antigen retrieval solution A and

B (cat. no. SBT10013; Shunbai Biotechnology Co., Ltd.; both incubated at 37˚C for 30 min), and the sections blocked with 3% hydrogen peroxide at room temperature for 10 min for 30 min. Triton X-100 (0.04%) was used to permeabilize the sections for 20 min at room temperature and goat serum (10%; cat. no. ZLI-9022; Beijing Zhongshan Jinqiao Biotechnology Co., Ltd.) was used to block the sections for 60 min at room temperature. Sections were incubated with the following primary antibodies: Anti-osteoprotegerin (OPG; 1:50; cat. no. ab73400; Abcam), anti-runt-related transcription factor 2 (RUNX2; 1:50; cat. no. ab236639; Abcam), Nrf2 polyclonal antibody (1:200; cat. no. 16396-1-AP; Proteintech Group, Inc.), Slc7a11 polyclonal antibody (1:50; cat. no. 26864-1-AP; Proteintech Group, Inc.) and Gpx4 monoclonal antibody (1:50; cat. no. 67763-1-Ig; Proteintech Group, Inc.) at 37˚C overnight. Sections were incubated with an HRP-conjugated goat anti-rabbit IgG secondary antibody (1:2000; cat. no. GB23204; Wuhan Servicebio Technology Co., Ltd.) at 37˚C for 120 min and biotinylated secondary antibodies (1:2,000; cat. no. PV-9001; Beijing Zhongshan Jinqiao Biotechnology Co., Ltd.) for 120 min at room temperature. For the comparative analysis of marker expression, additional sections were processed using optimized antibody concentrations and incubation conditions: primary antibody incubation at 37˚C for 1 h, followed by secondary antibody incubation at 37˚C for 20 min. The sections were treated with color developing solution (DAB Kit; cat. no. ZLI-9017; Beijing Zhongshan Jinqiao Biotechnology Co., Ltd.). The staining results were observed under a light microscope.

Dual immunofluorescence staining. Immunofluorescence staining was performed by binding fluorescently labeled secondary antibodies to primary antibodies to label corresponding proteins. Paraffin-embedded sections prepared as aforementioned were deparaffinized and rehydrated in absolute, 95 and 75% ethanol, then antigen retrieval was performed using antigen retrieval reagents A and B (both incubated at 37˚C for 30 min), endogenous peroxidase blocker was added and the sections were incubated in the dark at room temperature for 10 min. Subsequently, the sections were blocked with 10% rabbit serum (cat. no. ZLI-9026; Beijing Zhongshan Jinqiao Biotechnology Co., Ltd.) at room temperature for 30 min, and incubated with Gpx4 monoclonal antibody (1:50; cat. no. 67763-1-Ig; Proteintech Group, Inc.) and OCN antibody (1:100; cat. no. ab93876; Abcam) at 4˚C overnight. The corresponding fluorescent secondary antibodies (Alexa Fluor 488-conjugated goat anti-mouse IgG, 1:200, cat. no. ab150113, Abcam; Alexa Fluor 594-conjugated goat anti-rabbit IgG, 1:200, cat. no. ab150080, both Abcam) were added at room temperature for 50 min in the dark, followed by tyramide signal amplification reaction at room temperature for 10 min in the dark. Finally, DAPI staining was performed, the slices were dehydrated and blocked with anti-fade mounting medium and fluorescence was excited according to the corresponding wavelength of the dye using a fluorescence microscope.

Reverse transcription-quantitative polymerase chain reaction (RT-qPCR). The expression levels of genes related to ferroptosis were detected by RT-qPCR. Tibia samples were ground into powder in liquid nitrogen using a grinder, collected into centrifuge tubes and placed on ice. RNA was extracted from the tissue using the TRIzol® (Invitrogen; Thermo Fisher Scientific, Inc.) method according to standard operating procedures. RNA was reverse transcribed into cDNA using the PrimeScript RT reagent kit (Takara Bio, Inc.) according to the manufacturer's protocol. The primer sequences utilized for quantifying the expression levels of nuclear receptor coactivator 4 (Ncoa4), ferritin heavy chain (Fth), Nrf2, Slc7a11 and Gpx4 genes are provided in Table I. Amplification was performed using Hieff qPCR SYBR Green Master Mix (High Rox Plus; cat. no. 11203ES08; Shanghai Yeasen Biotechnology Co., Ltd.) under the following conditions: Initial denaturation at 95˚C for 30 sec, followed by 40 cycles of denaturation at 95˚C for 5 sec and annealing/extension at 60˚C for 20 sec. Gene expression levels were quantified using the $2^{-\Delta\Delta Cq}$ method (27), with Gapdh as the reference gene for data normalization.

Statistical analysis. SPSS v.26.0 (IBM Corp.) was used for data analysis. All of the obtained data are presented as the mean ± standard deviation. Groups were compared using one-way ANOVA followed by Tukey's post hoc test. $P<0.05$ was considered to indicate a statistically significant difference.

Results

Main components of YC. The main components of YC were determined using UPLC-MS/MS and the results are shown in Fig. 1 according to the relative content of various compounds. A total of 2,072 compounds were identified, which were divided into 13 categories, including 333 phenolic acids, 308 flavonoids, 259 amino acids and their derivatives, 233 alkaloids, 205 lipids, 134 lignans and coumarin, 127 organic acids, 113 terpenoids, 69 nucleotides and their derivatives, 23 quinones, 16 steroids, 5 tannins and 247 others. The main active ingredients of YC included chlorogenic acid, ferulic acid, caffeic acid, artemisininolide, artemisinin, scopoletin, quercetin, hyperoside, isorhamnetin and isoquercitrin (data not shown). The 10 compounds listed in Table II were selected based on their documented anti-osteoporotic activities in previous literature and their relative abundance in the extract (5,9,10,28).

Effect of YC on weight change, uterine coefficient and serum estradiol in OVX mice. In the present study, as shown in Fig. 2, OVX mice had significantly lower serum estradiol levels compared with those in SHAM mice. OVX mice also showed a significant increase in body weight and a significantly lower uterine coefficient compared with those in the SHAM group. Notably, the administration of YC significantly reversed these changes in body weight and estradiol levels, although no significant difference in uterine coefficient was observed between the OVX and YC groups. EV treatment also significantly increased the uterine coefficient compared with the OVX group. However, there were no significant differences observed between the YCL and YCH groups.

Effect of YC on femoral bone microstructure in OVX mice. Micro-CT analysis was used to investigate the effect of YC

Table I. Primer sequence.

Gene	Forward, 5'-3'	Reverse, 5'-3'
Ncoa4	CCCTTCCAGAAATGAGCTAACA	GCCACTCTGACAAGGAACTATT
Fth	TGACCACGTGACCAACTTAC	CGTCAGCTTAGCTCTCATCAC
Nrf2	GGCTCAGCACCTTGTATCTT	CACATTGCCATCTCTGGTTTG
Slc7a11	CTGGTCAGCCAGCTTATGAA	AGGAGGATGCTGCCAATAAC
Gpx4	TGTGCATCCCGCGATGATT	CCCTGTACTTATCCAGGCAGA
Gapdh	GAATGGGAAGCTGGTCATCAA	CCAGTAGACTCCACGACATACT

Ncoa4, nuclear receptor coactivator 4; Fth, ferritin heavy chain; Nrf2, nuclear factor erythroid 2-related factor 2; Slc7a11, solute carrier family 7 member 11; Gpx4, glutathione peroxidase 4.

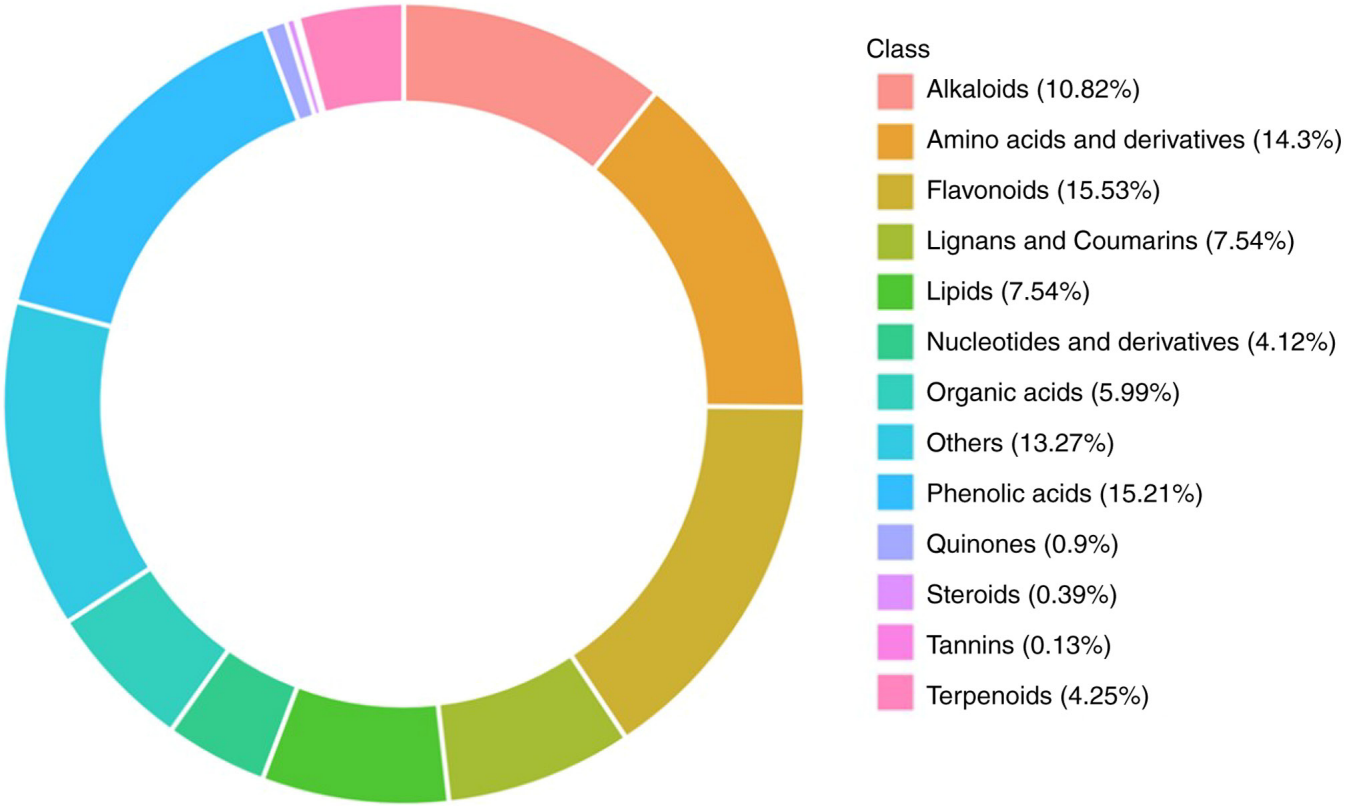

Figure 1. Ring diagram of the composition of the metabolite categories of YC.

on bone microstructure in OVX mice. As shown in Fig. 3A, the femoral trabeculae of mice in the SHAM group were thick, closely arranged and continuous, whereas the number of femoral trabeculae of mice in the OVX group was markedly reduced, the bone microstructure was broken, and the number and sizes of gaps increased. Both EV and YC treatment markedly improved the deteriorated trabecular structure observed in OVX mice. As shown in Fig. 3B-F morphometric parameters further supported the observed changes in trabecular microstructure in the different groups. Consistent with the scanned images, OVX mice had significantly reduced BMD, BV/TV and Tb.N compared with those in the SHAM group, whereas SMI and Tb.Sp were significantly increased. However, the independent application of YC and estradiol significantly ameliorated these changes.

Effect of YC on the pathological morphology of femurs in OVX mice. To further evaluate the effect of YC on trabecular structure, H&E staining was performed on the femurs of mice. As shown in Fig. 4A, a well-organized trabecular meshwork and a small bone marrow cavity were observed in the SHAM group. However, in the OVX group, it was found that the bone marrow cavity was enlarged, the trabecular structure was disordered and the lipid droplets in the bone marrow were markedly increased. H&E staining also showed that EV and YC ameliorated the histopathological changes in bone structure caused by ovariectomy. Masson's staining in Fig. 4B showed that, compared with in the SHAM group, the femoral bone trabeculae of the OVX group were thinner and more sparsely arranged, with increased spacing and less collagen. These changes were notably ameliorated in the EV and YC groups.

Table II. Relative content of the active components of Yinchen.

Chemical compound	Molecular formula	Category	Retention time, min	Relative content
Caffeic acid	$C_9H_8O_4$	Phenolic acids	3.4	2136.26
Ferulic acid	$C_{10}H_{10}O_4$	Phenolic acids	4	1277.59
Chlorogenic acid	$C_{16}H_{18}O_9$	Phenolic acids	2.7	737.32
Scopoletin	$C_{10}H_8O_4$	Lignans and coumarin	4.1	659.48
Isoquercitrin	$C_{21}H_{20}O_{12}$	Flavone	4	247.29
Artemisinin	$C_{11}H_{10}O_4$	Lignans and coumarin	5	97.44
Quercetin	$C_{15}H_{10}O_7$	Flavone	5.1	74.37
Chromenone	$C_{16}H_{12}O_7$	Lignans and coumarin	5.8	57.39
Isorhamnetin	$C_{16}H_{12}O_7$	Flavone	5.8	9.02
Hyperoside	$C_{21}H_{20}O_{12}$	Flavone	3.6	1.00

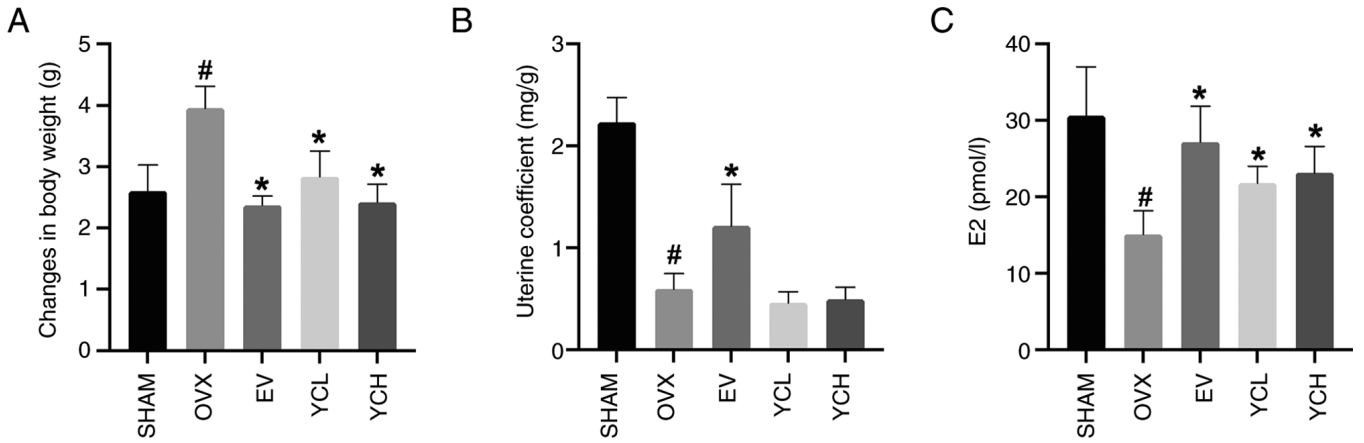

Figure 2. Effect of YC on body weight, E2 levels and uterine coefficient in OVX mice. (A) Changes in body weight. (B) Uterine coefficient of mice. (C) E2 levels in mice. Data are presented as mean ± SD; n=8. #P<0.05 vs. SHAM group; *P<0.05 vs. OVX group. YC, Yinchen; OVX, ovariectomized; EV, estradiol valerate; YCL, YC low dose; YCH, YC high dose; E2, estradiol.

Effect of YC on bone metabolism in OVX mice. The anti-osteoporotic effect of YC was monitored by detecting the serum levels of TRAP and OCN through ELISA, the results of which were shown in Fig. 5A and B. Compared with those in the SHAM group, the serum levels of TRAP and OCN in the OVX group were significantly increased (both P<0.05). These results indicated that ovariectomy resulted in an increased turnover rate of bone metabolism, whereas EV and YC significantly reduced the concentrations of these serum markers compared with those in the OVX group. However, there was no significant difference observed between the YCL and YCH groups.

Subsequently, femurs were subject to immunohistochemical staining, with RUNX2 and OPG being the key factors regulating the dynamic balance of bone tissue (29,30). As shown in Fig. 5C-F, the expression of OPG and RUNX2 in the OVX group was significantly lower than that in the SHAM group. Ovariectomy reduced bone formation in mice, whereas the EV and YC groups significantly increased the expression of OPG and RUNX2. The expression of RUNX2 in the femur of the YCH group was higher than that of the YCL group, but the difference was not statistically significant.

The osteoblast-specific marker OCN and ferroptosis inhibitor Gpx4 were co-stained by immunofluorescence staining to observe the expression of Gpx4 in femoral osteoblasts (Fig. 5G and H). Compared with in the SHAM group, the expression of Gpx4 in the femoral osteoblasts of OVX mice was significantly decreased, whereas EV and YC treatment significantly increased Gpx4 expression levels.

Effect of YC on iron metabolism in OVX mice. The liver is the main iron storage organ and when iron accumulates, the liver exhibits increased iron deposition (31). The iron ion content of liver sections was determined by Prussian blue staining (Fig. 6A). Compared with that in the Sham group, OVX mice demonstrated more punctate staining and heavier iron deposition in the liver, which was effectively reduced in the EV and YC groups.

Ferritin and hepcidin levels were subsequently measured by ELISA, whereas Ncoa4 and Fth mRNA expression levels were measured by RT-qPCR; the results of these assays were shown in Fig. 6B-E. Compared with those in the SHAM group, the levels of ferritin, hepcidin and Ncoa4 were significantly increased in OVX mice whereas the expression of Fth was significantly decreased. However, EV and YC administration significantly reversed these changes (all P<0.05).

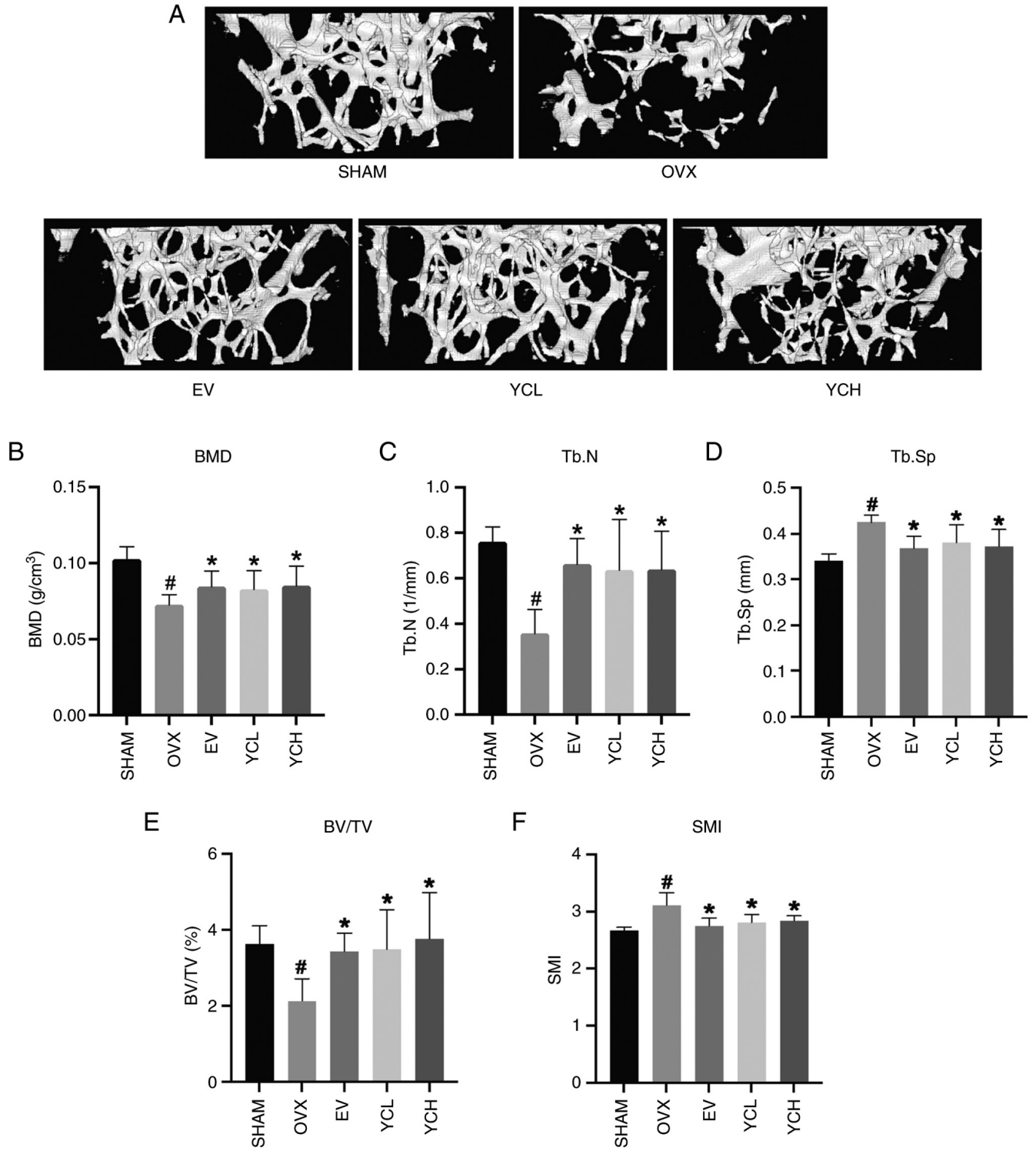

Figure 3. Effect of YC on femoral bone microstructure in OVX mice. (A) Micro-CT scanning images of bone microstructure. Changes in (B) BMD, (C) Tb.N, (D) Tb.Sp, (E) BV/TV and (F) SMI. Data are presented as the mean ± SD; n=8. #P<0.05 vs. SHAM group; *P<0.05 vs. OVX group. OVX, ovariectomized; EV, estradiol valerate; YC, Yinchen; YCL, YC low dose; YCH, YC high dose; BMD, bone mineral density; Tb.N, trabecular number; Tb.Sp, trabecular separation; BV/TV, bone volume/total volume; SMI, structure model index.

Effect of YC on lipid peroxidation in OVX mice. Lipid peroxidation is an important link in ferroptosis, and the accumulation of lipid peroxides in the local membrane is the key reaction leading to cell death (32). MDA, 4-HNE and GSH contents in the tibias and sera of mice were measured by ELISA (Fig. 7). Compared with those in the SHAM mice, the levels of MDA and 4-HNE were significantly increased in OVX mice, whereas the levels of GSH were significantly decreased. EV and YC significantly reversed the changes in MDA, 4-HNE and GSH in the serum and tibias after ovariectomy.

Effect of YC on the Nrf2/Slc7a11/Gpx4 pathway. The expression levels of Nrf2, Slc7a11 and Gpx4 in the bone tissue of mice were detected by RT-qPCR and immunohistochemistry

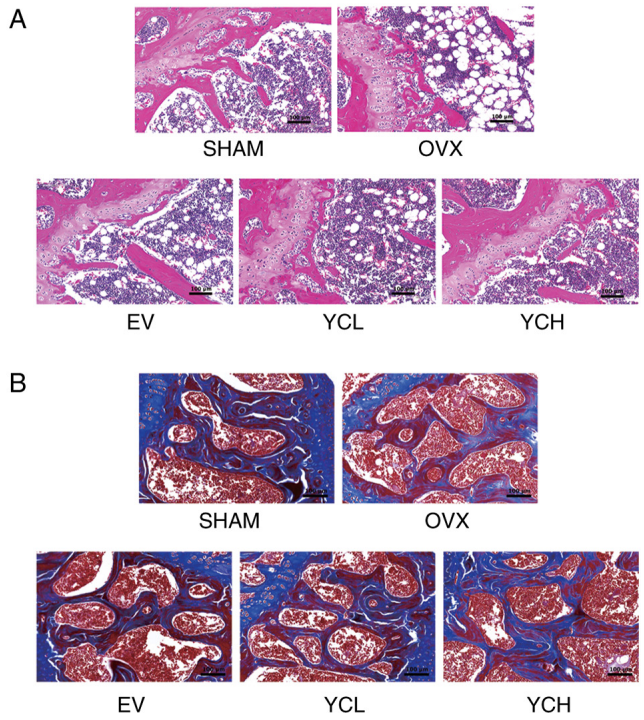

Figure 4. Effect of YC on the pathological morphology of femurs in OVX mice. Image analysis (x200 magnification) of (A) Hematoxylin and eosin staining and (B) Masson's trichrome staining. OVX, ovariectomized; EV, estradiol valerate; YC, Yinchen; YCL, YC low dose; YCH, YC high dose.

(Fig. 8). Compared with those in the SHAM group, the mRNA and protein expression levels of Nrf2, Slc7a11 and Gpx4 in the bone tissue of OVX mice were significantly decreased. By contrast, compared with those in the OVX mice, EV and YC treatment significantly increased their expression levels.

Discussion

In the present study, UPLC-MS/MS was used to detect the active components of YC. The OVX osteoporotic mouse model was used to simulate PMOP, and the effects and mechanism of YC in the treatment of osteoporosis were explored. Reduced estrogen levels lead to a gradual decrease in osteoblast number and activity, resulting in a reduced rate of bone formation (26). When osteoporosis occurs, BMSCs are more likely to transform into adipocytes than in healthy individuals (33). In the present study, estradiol levels in the serum of YC-treated mice were increased and mouse body weight was decreased, indicating that YC improved the reduction of estrogen levels and body weight gain caused by ovariectomy, but could not restore the uterine atrophy caused by ovariectomy, as indicated by the lack of significant difference in uterine coefficient. In addition, in OVX mice, the trabecular bone destruction was notable, the formation of lipid droplets in the bone marrow cavity increased and bone formation decreased.

TRAP and OCN are serum markers of bone turnover (34). Increased levels of bone turnover markers may precede changes in BMD. In OVX mice, the present study detected elevated levels of TRAP and OCN in mouse serum. RUNX2 is a key osteogenic transcription factor. In immature osteoblasts, RUNX2 can regulate the expression of bone matrix proteins, such as secreted phosphoprotein 1, collagen type I α1, collagen type I α2 and OCN, and can induce the maturation of osteoblasts (35,36). OPG is secreted by osteoblasts and can competitively bind to RANKL. It also inhibits the binding of RANKL to RANK. OPG-null mice exhibit reduced whole-body BMD, whereas the use of RANKL inhibitors can enhance Wnt/β-catenin signaling and induce bone formation in OPG null mice (37,38). Immunohistochemistry showed that the expression levels of OPG and RUNX2 were decreased in the femurs of OVX mice compared with those in the Sham group, indicating that bone formation was inhibited in the bone tissue of mice with ovariectomy-induced osteoporosis, whereas the administration of YC was shown to promote the expression of osteogenesis-related factors in bone tissue.

Ferroptosis is a novel mode of cell death characterized by iron accumulation and lipid peroxidation. Ferroptosis is involved in high-fat-induced bone loss, and ferroptosis in high-fat-fed osteoporotic mice can be inhibited by intraperitoneal injection of ferrostatin-1 (39). In a mouse model of diabetic osteoporosis, the levels of lipid peroxides in the body are increased and the levels of osteogenic markers are decreased (40). Another study found that type 2 diabetes can reduce the expression of mitochondrial ferritin in bone tissue and cause ferroptosis (41). Serum levels of the ferroptosis markers Gsh, Gpx4 and MDA can more effectively predict the occurrence of PMOP compared to conventional bone turnover markers such as OCN and C-terminal telopeptide of type I collagen. Iron overload occurs in postmenopausal women, and the increase in iron levels after menopause may be related to the loss of the pathway of menstrual blood loss to expel ferritin (42,43). This implies that ferroptosis may be an important mechanism in the pathogenesis of osteoporosis.

Hepcidin is the core factor regulating the balance of iron metabolism, and the level of hepcidin is regulated by the feedback of iron level in the body. Hepcidin-knockout mice display increased serum iron and ferritin content, increased liver and bone iron content and inhibited osteogenic differentiation (44,45). Ferritin is the predominant iron storage protein in cells, which is composed of Fth and ferritin light chain. Fth is the principal iron-storing subunit of ferritin. In a state of iron deficiency, Ncoa4 can recognize and bind to Fth, degrade Fth, release iron ions into cells, promote lipid peroxidation and induce ferroptosis (46). The etiology of osteoporosis is notably associated with the overproduction of lipid peroxides, which represents the terminal stage of ferroptosis (47). In the present study, serum ferritin levels were elevated in OVX mice, indicating that iron accumulation has occurred. At the same time, the liver iron ion level of OVX mice was notably increased.

Ncoa4 can promote the degradation of Fth and release iron ions into the cells, which is a process involved in ferroptosis (32). Therefore, the present study examined the expression levels of Ncoa4 and Fth in the tibia of OVX mice; RT-qPCR analysis revealed that Ncoa4 was found to be significantly increased, whereas Fth levels were decreased in OVX mice compared with the Sham group. On the other hand, lipid peroxidation is an important feature of ferroptosis. Excess intracellular iron participates in the production of peroxide and then participates in the formation of lipid peroxide with polyunsaturated fatty acids (48). The significant increase in MDA and 4-HNE

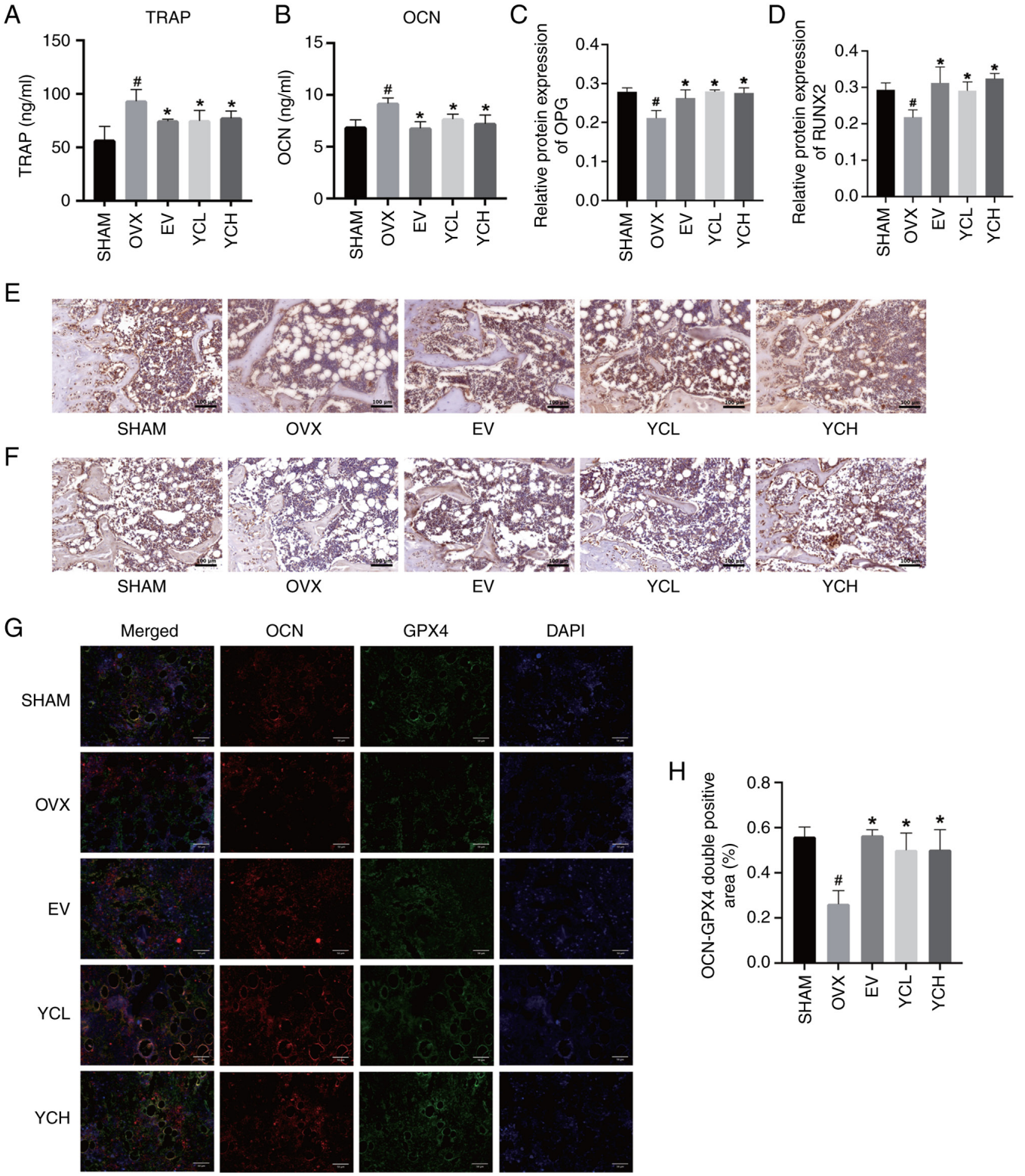

Figure 5. Effect of YC on bone metabolism in OVX mice. Results of (A) TRAP and (B) OCN ELISA. Relative protein expression levels of (C) OPG and (D) RUNX2. Immunohistochemical staining of (E) OPG and (F) RUNX2 protein expression (x200 magnification). (G) Double immunofluorescence staining images of OCN and GPX4 (x400 magnification). (H) OCN-GPX4 double positive area. Data are presented as the mean ± SD; n=8. $^{\#}$P<0.05 vs. SHAM group; *P<0.05 vs. OVX group. OVX, ovariectomized; EV, estradiol valerate; YC, Yinchen; YCL, YC low dose; YCH, YC high dose; TRAP, tartrate-resistant acid phosphatase; OCN, osteocalcin; OPG, osteoprotegerin; RUNX2, runt-related transcription factor 2; GPX4, glutathione peroxidase 4.

levels, and decrease in GSH levels in the serum and bone tissues of OVX mice compared with in the SHAM mice in the present study indicated that lipid peroxidation was elevated in the OVX mice. The results of immunofluorescence double staining of OCN and Gpx4 showed that the co-staining area of OCN and Gpx4 in the femurs of OVX mice was significantly reduced compared with that in the SHAM mice, indicating that Gpx4 expression was decreased, and the level of iron

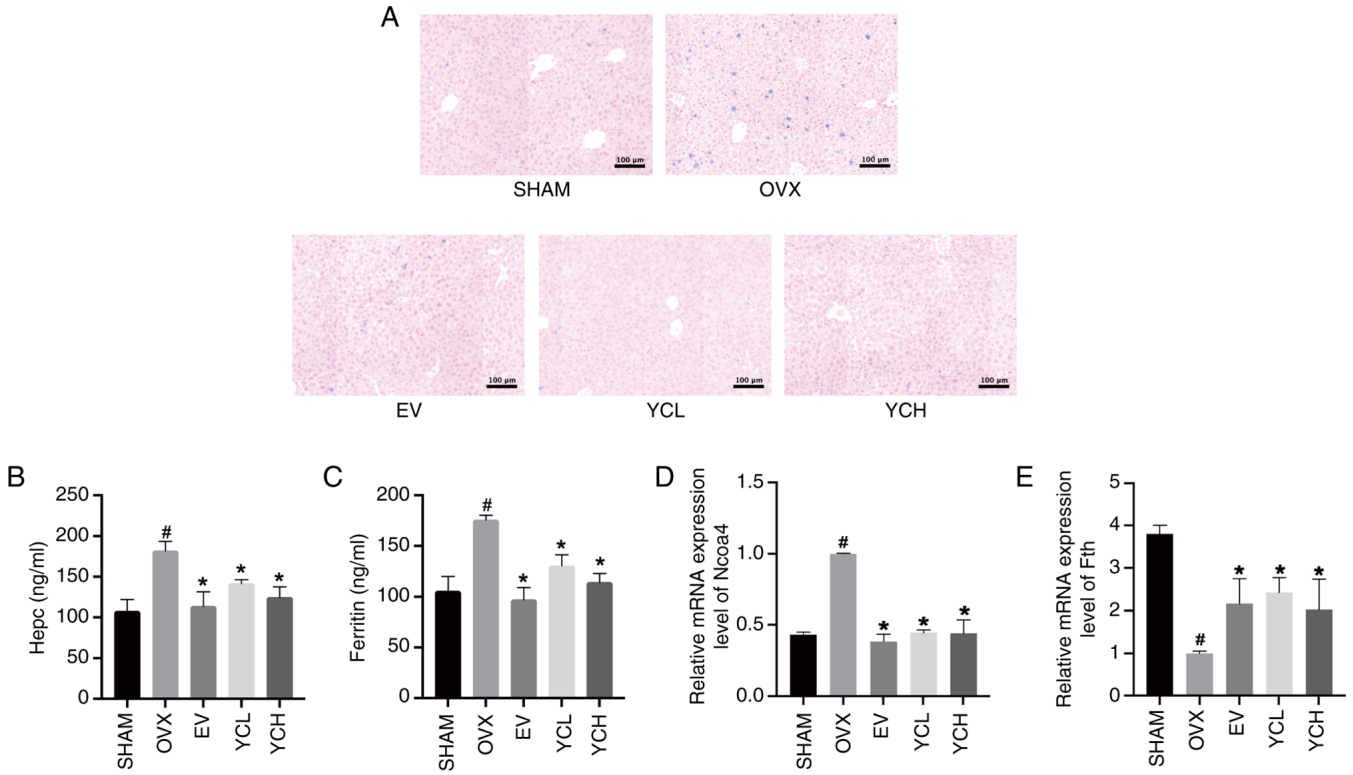

Figure 6. Effect of YC on iron metabolism in OVX mice. (A) Prussian blue staining image of mouse livers (x200 magnification). (B) Hepc and (C) ferritin Levels. Relative mRNA expression levels of (D) Ncoa4 and (E) Fth. Data are presented as the mean ± SD; n=8. #P<0.05 vs. SHAM group; *P<0.05 vs. OVX group. OVX, ovariectomized; EV, estradiol valerate; YC, Yinchen; YCL, YC low dose; YCH, YC high dose; Hepc, hepcidin; Ncoa4, nuclear receptor coactivator 4; Fth, ferritin heavy chain.

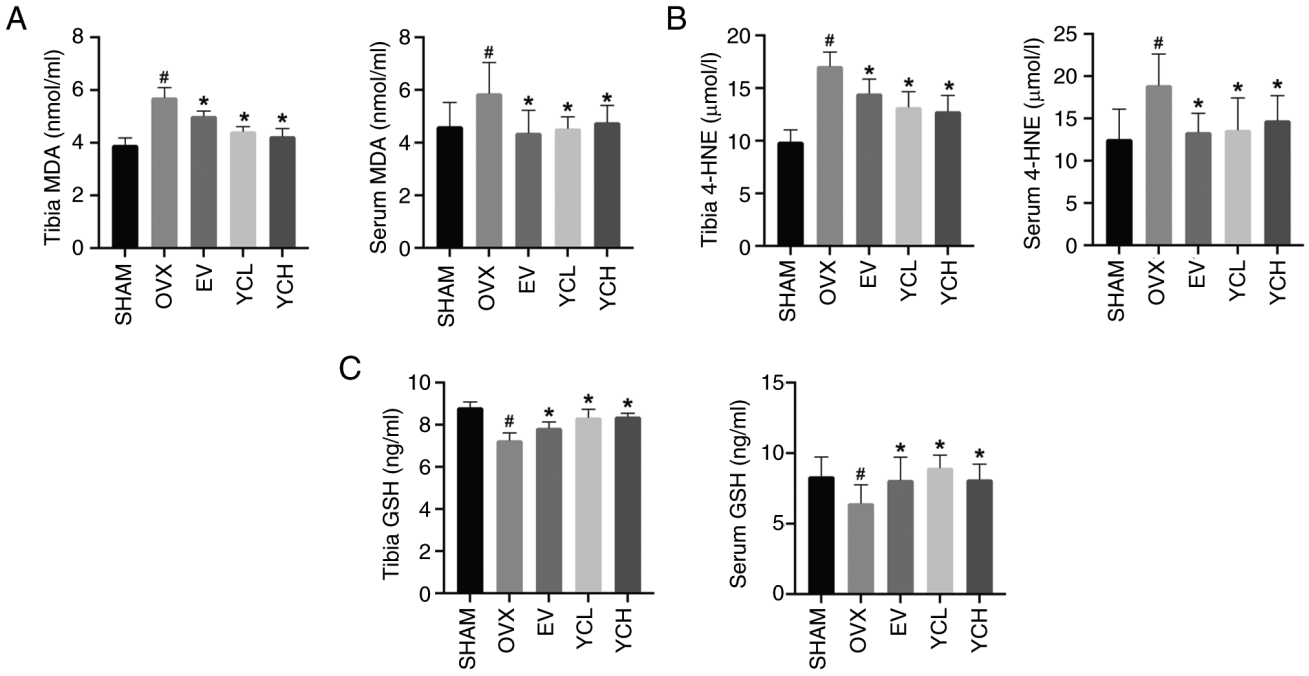

Figure 7. Effect of YC on lipid peroxidation in OVX mice. Tibia and serum levels of (A) MDA, (B) 4-HNE and (C) GSH. Data are presented as the mean ± SD; n=8. #P<0.05 vs. SHAM group; *P<0.05 vs. OVX group. OVX, ovariectomized; EV, estradiol valerate; YC, Yinchen; YCL, YC low dose; YCH, YC high dose; MDA, malondialdehyde; 4-HNE, 4-hydroxynonenal; GSH, glutathione.

accumulation and lipid peroxidation in the OVX mice was increased, which suggested that the bone tissue of OVX mice exhibited ferroptosis.

Upon treatment with YC, mice displayed the following changes compared with OVX mice: i) Serum ferritin and hepcidin levels, and liver iron ion content were decreased;

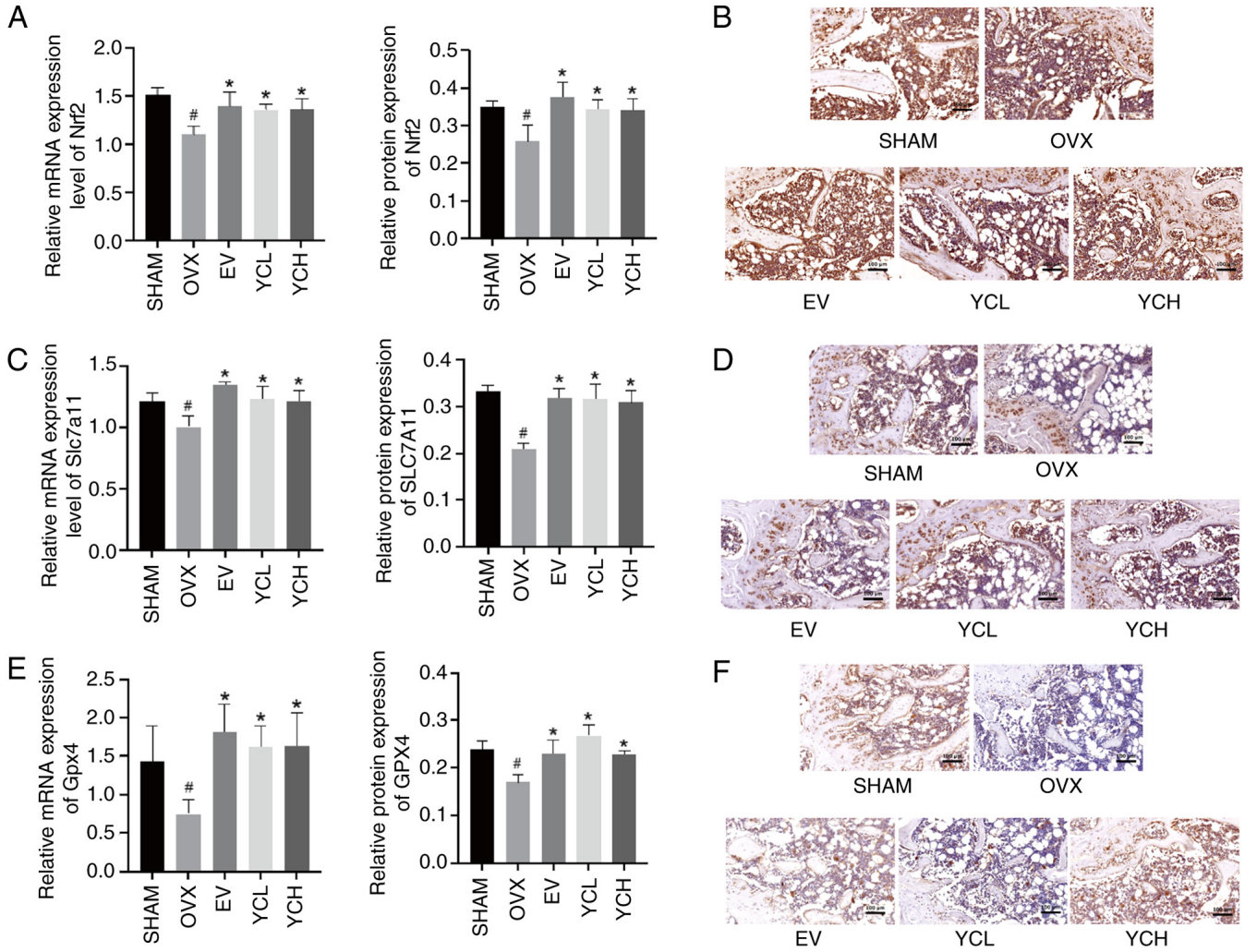

Figure 8. Effect of YC on the Nrf2/Slc7a11/Gpx4 pathway. (A) Relative mRNA and protein expression levels of Nrf2. (B) Immunohistochemical images of Nrf2 in mouse femurs (x200 magnification). (C) Relative mRNA and protein expression levels of Slc7a11. (D) Immunohistochemical images of Slc7a11 in mouse femurs (x200 magnification). (E) Relative mRNA and protein expression levels of Gpx4. (F) Immunohistochemical images of Gpx4 in mouse femurs (x200 magnification). Data are presented as the mean ± SD; n=8. $^{\#}$P<0.05 vs. SHAM group; *P<0.05 vs. OVX group. OVX, ovariectomized; EV, estradiol valerate; YC, Yinchen; YCL, YC low dose; YCH, YC high dose; Nrf2, nuclear factor erythroid 2-related factor 2; Slc7a11, solute carrier family 7 member 11; Gpx4, glutathione peroxidase 4.

ii) Ncoa4 expression in bone tissue was decreased; iii) the expression levels of Fth in bone tissue was increased; iv) MDA and 4-HNE levels in serum and bone tissue were decreased; v) GSH levels were increased; and Gpx4 expression was increased. These results suggested that YC improved osteoporosis in OVX mice by inhibiting ferroptosis.

Nrf2 is a key regulator of cellular antioxidant responses, which drive transcriptional responses that inhibit ferroptosis (26,49). Under physiological conditions, Nrf2 is maintained at low levels in the cytoplasm by interacting with Kelch-like ECH-associated protein 1 (Keap1) to form a complex. Under oxidative stress, Keap1 is degraded by autophagy and Nrf2 is released into the cytoplasm. Subsequently, free Nrf2 is transported to the nucleus where it binds to antioxidant response elements and initiates downstream reactions (26). Nrf2 can regulate factors related to GSH synthesis and metabolism, including the catalytic and regulatory subunits of glutamate-cysteine ligase, GSH synthetase and the system xc^- subunits Slc7a11 and Gpx4 (24). Thus, Nrf2 is a key repressor of the ferroptosis response. In pancreatic cancer cells, Nrf2 can activate microsomal GSH S-transferase 1, inhibiting lipoxygenase 5 (Alox5) and ferroptosis (50). Studies have confirmed that increased Nrf2 expression can inhibit ferroptosis and that downregulation of Nrf2 expression can increase the sensitivity of cells to ferroptosis (26,51). The results of the present study showed that this pathway was inhibited in OVX mice. By contrast, YC increased the expression of Gpx4 and OCN in OVX mouse osteoblasts and activated the Nrf2/Slc7a11/Gpx4 pathway. Previous studies have confirmed that kakaferol can enhance cellular antioxidant capacity, inhibit the accumulation of lipid peroxides in neurons and inhibit ferroptosis by activating the Nrf2/Slc7a11/Gpx4 pathway; pachynic acid has also been shown to inhibit oxygen-glucose deprivation/re-oxygenation-induced lipid peroxidation and ferroptosis in cardiomyocytes by activating this pathway (26,52). Taken together, it can be inferred that YC may inhibit osteoblast ferroptosis by activating the Nrf2/Slc7a11/Gpx4 pathway, thereby promoting bone formation and improving osteoporosis in OVX mice. While YC may exert its effects through multiple pathways, the present

study focused on the Nrf2/Slc7a11/Gpx4 axis due to its established role in ferroptosis and bone metabolism. Future studies should investigate other potential pathways, such as HO-1 and RANKL-mediated osteoclast differentiation, to provide an improved comprehensive mechanistic understanding of the effects of YC on osteoporosis.

In addition, Nrf2 is a key transcription factor that regulates cellular antioxidant responses and iron metabolism. It modulates susceptibility to ferroptosis by regulating the expression of a series of downstream genes, including several directly involved in ferroptosis. For example, Fth1 facilitates iron storage, reducing the intracellular labile iron pool and thereby attenuating ferroptotic cell death. Similarly, Gpx4 is a notable enzyme that suppresses lipid peroxidation and Nrf2 can upregulate Gpx4 expression to inhibit ferroptosis (53,54). Based on the association between the Nrf2 pathway and ferroptosis, the present study investigated the regulatory role of YC in this pathway (55).

The present study had a number of limitations to be acknowledged. Primarily, the causal relationship between YC treatment and the activation of the Nrf2 pathway was not directly validated through genetic or pharmacological interventions in the present study, with the inference primarily relying on changes in biomarker expression and existing literature. Furthermore, although UPLC-MS/MS identified numerous compounds, the synergistic or antagonistic interactions among the constituents within the YC extract remain unexplored and the exact bioactive components responsible for the observed effects require further isolation and functional verification. Additionally, biomechanical assessments, such as the three-point bending test, were not performed to evaluate bone strength improvement. Finally, while the dosage used in the present study (5-10 g/kg) is within the range of clinical applications of YC in traditional Chinese medicine, which can reach up to 100 g/day in human patients (56,57), chronic toxicity and comprehensive safety profiles of YC at these doses were not systematically investigated, which are important for evaluating its clinical translational potential. Future studies employing Nrf2-knockout models and ferroptosis inducers are warranted to conclusively establish the causal role of the Nrf2/Slc7a11/Gpx4 axis in mediating the anti-osteoclastogenic effects of YC while the incorporation of functional biomechanical tests and component-specific approaches will be important to fully elucidate the therapeutic potential of YC for bone disorders.

In conclusion, the present study suggested the effectiveness of YC in potentially mitigating ovariectomy-induced osteoporosis in mice. YC promoted bone formation and improved bone microstructure by potentially inhibiting ferroptosis via activation of the Nrf2/Slc7a11/Gpx4 pathway in OVX mice.

Acknowledgements

Not applicable.

Funding

The present work was supported by the National Natural Science Foundation of China (grant no. 82074297) and the Fundamental Research Funds for the Central Public Welfare Research Institutes (grant nos. YZ-202244, YZX202335 and YZX202235).

Availability of data and materials

The data generated in the present study may be requested from the corresponding author. The UPLC-MS/MS data generated in the present study may be found in the MetaboLights public database under accession number MTBLS13042 or at the following URL: https://www.ebi.ac.uk/metabolights/editor/MTBLS13042).

Authors' contributions

PL and ZZ conceived the study. PL, YC and ZZ contributed to the methodology development. WL performed the experiments. XW, YY and DC analyzed data. PL wrote the manuscript. RZ made substantial contributions to the interpretation of data and critically revised the manuscript for important intellectual content. ZZ and HL also participated in critical revision of the manuscript. YW contributed to project administration, participated in data interpretation and revised the manuscript. HL supervised the overall research design, interpreted the key results and acquired the funding. All authors have read and approved the final manuscript. PL and XW confirm the authenticity of all the raw data.

Ethics approval and consent to participate

All animal experiments were performed in strict accordance with the ethical guidelines of the Institute of Basic Theory for Chinese Medicine, China Academy of Chinese Medical Sciences, and were approved by the Institutional Animal Ethics Committee (approval no. IBTCMCACMS21-2303-04). Efforts were made to minimize animal suffering and reduce the number of animals used.

Patient consent for publication

Not applicable.

Competing interests

The authors declare that they have no competing interests.

References

1. Garnero P, Sornay-Rendu E, Duboeuf F and Delmas PD: Markers of bone turnover predict postmenopausal forearm bone loss over 4 years: The OFELY study. J Bone Miner Res 14: 1614-1621, 1999.
2. Hernlund E, Svedbom A, Ivergård M, Compston J, Cooper C, Stenmark J, McCloskey EV, Jönsson B and Kanis JA: Osteoporosis in the European union: Medical management, epidemiology and economic burden. A report prepared in collaboration with the International Osteoporosis Foundation (IOF) and the European Federation of Pharmaceutical Industry Associations (EFPIA). Arch Osteoporos 8: 136, 2013.
3. An J, Yang H, Zhang Q, Liu C, Zhao J, Zhang L and Chen B: Natural products for treatment of osteoporosis: The effects and mechanisms on promoting Osteoblast-mediated bone formation. Life Sci 147: 46-58, 2016.
4. Lee CJ, Shim KS and Ma JY: *Artemisia capillaris* alleviates bone loss by stimulating osteoblast mineralization and suppressing osteoclast differentiation and bone resorption. Am J Chin Med 44: 1675-1691, 2016.
5. Lee SH, Lee JY, Kwon YI and Jang HD: Anti-Osteoclastic activity of *Artemisia capillaris* thunb. Extract depends upon attenuation of osteoclast differentiation and bone Resorption-associated acidification due to chlorogenic acid, hyperoside, and scoparone. Int J Mol Sci 18: 322, 2017.

6. Liu YP, Qiu XY, Liu Y and Ma G: Research progress on the pharmacological effects of *Artemisiae Scopariae Herba*. Chinese Traditional and Herbal Drugs 50: 2235-2241, 2019 (In Chinese).
7. Witaicenis A, Seito LN, Da Silveira Chagas A, de Almeida LD Jr, Luchini AC, Rodrigues-Orsi P, Cestari SH and Di Stasi LC: Antioxidant and intestinal Anti-inflammatory effects of Plant-derived coumarin derivatives. Phytomedicine 21: 240-246, 2014.
8. Zeinali M and Rezaee SA and Hosseinzadeh H: An overview on immunoregulatory and Anti-inflammatory properties of chrysin and flavonoids Substances. Biomed Pharmacother 92: 998-1009, 2017.
9. Gupta A, Atanasov AG, Li Y, Kumar N and Bishayee A: Chlorogenic acid for cancer prevention and therapy: Current status on efficacy and mechanisms of Action. Pharmacol Res 186: 106505, 2022.
10. Ding J, Wang L, He C, Zhao J, Si L and Huang H: *Artemisia scoparia*: Traditional uses, active constituents and pharmacological effects. J Ethnopharmacol 273: 113960, 2021.
11. Gan DL, Yao Y, Su HW, Huang YY, Shi JF, Liu XB and Xiang MX: Volatile oil of *Platycladus orientalis* (L.) Franco leaves exerts strong Anti-inflammatory effects via inhibiting the IκB/NF-κB pathway. Curr Med Sci 41: 180-186, 2021.
12. Zhou RP, Deng MT, Chen LY, Fang N, Du C, Chen LP, Zou YQ, Dai JH, Zhu ML, Wang W, *et al*: Shp2 regulates chlorogenic acid-induced proliferation and adipogenic differentiation of bone Marrow-derived mesenchymal stem cells in adipogenesis. Mol Med Rep 11: 4489-4495, 2015.
13. Xu T, Wu X, Zhou Z, Ye Y, Yan C, Zhuge N and Yu J: Hyperoside ameliorates periodontitis in rats by promoting osteogenic differentiation of BMSCs via activation of the NF-κB pathway. FEBS Open Bio 10: 1843-1855, 2020.
14. Han D, Chen W, Gu X, Shan R, Zou J, Liu G, Shahid M, Gao J and Han B: Cytoprotective effect of chlorogenic acid against hydrogen Peroxide-induced oxidative stress in MC3T3-E1 cells through PI3K/Akt-mediated Nrf2/HO-1 signaling pathway. Oncotarget 8: 14680-14692, 2017.
15. Folwarczna J, Pytlik M, Zych M, Cegieła U, Nowinska B, Kaczmarczyk-Sedlak I, Sliwinski L, Trzeciak H and Trzeciak HI: Effects of caffeic and chlorogenic acids on the rat skeletal system. Eur Rev Med Pharmacol Sci 19: 682-693, 2015.
16. Kwak SC, Lee C, Kim JY, Oh HM, So HS, Lee MS, Rho MC and Oh J: Chlorogenic acid inhibits osteoclast differentiation and bone resorption by down-regulation of receptor activator of nuclear factor kappa-B ligand-induced nuclear factor of activated T cells c1 expression. Biol Pharm Bull 36: 1779-1786, 2013.
17. Lee SH and Jang HD: Scoparone attenuates RANKL-induced osteoclastic differentiation through controlling reactive oxygen species production and scavenging. Exp Cell Res 331: 267-277, 2015.
18. An H, Chu C, Zhang Z, Zhang Y, Wei R, Wang B, Xu K, Li L, Liu Y, Li G and Li X: Hyperoside alleviates postmenopausal osteoporosis via regulating miR-19a-5p/IL-17A axis. Am J Reprod Immunol 90: e13709, 2023.
19. Lee SH, Ding Y, Yan XT, Kim YH and Jang HD: Scopoletin and scopolin isolated from *Artemisia iwayomogi* suppress differentiation of osteoclastic macrophage RAW 264.7 cells by scavenging reactive oxygen species. J Nat Prod 76: 615-620, 2013.
20. Dixon SJ, Lemberg KM, Lamprecht MR, Skouta R, Zaitsev EM, Gleason CE, Patel DN, Bauer AJ, Cantley AM, Yang WS, *et al*: Ferroptosis: An iron-dependent form of nonapoptotic cell death. Cell 149: 1060-1072, 2012.
21. Bersuker K, Hendricks JM, Li Z, Magtanong L, Ford B, Tang PH, Roberts MA, Tong B, Maimone TJ, Zoncu R, *et al*: The CoQ oxidoreductase FSP1 acts parallel to Gpx4 to inhibit ferroptosis. Nature 575: 688-692, 2019.
22. Kraft VAN, Bezjian CT, Pfeiffer S, Ringelstetter L, Müller C, Zandkarimi F, Merl-Pham J, Bao X, Anastasov N, Kössl J, *et al*: GTP Cyclohydrolase 1/Tetrahydrobiopterin Counteract ferroptosis through lipid remodeling. ACS Cent Sci 6: 41-53, 2020.
23. Stockwell BR, Friedmann Angeli JP, Bayir H, Bush AI, Conrad M, Dixon SJ, Fulda S, Gascón S, Hatzios SK, Kagan VE, *et al*: Ferroptosis: A regulated cell death nexus linking metabolism, redox biology, and disease. Cell 171: 273-285, 2017.
24. Dodson M, Castro-Portuguez R and Zhang DD: NRF2 plays a critical role in mitigating lipid peroxidation and Ferroptosis. Redox Biol 23: 101107, 2019.
25. Jiang Z, Qi G, He X, Yu Y, Cao Y, Zhang C, Zou W and Yuan H: Ferroptosis in osteocytes as a target for protection against postmenopausal osteoporosis. Adv Sci (Weinh) 2024: e2307388, 2024.
26. Sun X, Ou Z, Chen R, Niu X, Chen D, Kang R and Tang D: Activation of the p62-Keap1-NRF2 pathway protects against ferroptosis in hepatocellular carcinoma cells. Hepatology 63: 173-184, 2016.
27. Livak KJ and Schmittgen TD: Analysis of relative gene expression data using real-time quantitative PCR and the 2(-Delta Delta C(T)) method. Methods 25: 402-408, 2001.
28. Kim TE, Jo YH and Kim CT: Improvement of quality characteristics of mulberry (*Morus alba* L.) fruit extract using high-pressure enzymatic treatment. Food Bioprocess Technol 17: 4106-4114, 2024.
29. Gnoumou E, Tran TA, Yang TT, Quach TT and Wang CY: Antibacterial, anti-inflammatory and anti-osteoclastogenic effects of synthetic mineralized lysozyme nanoparticles for treating infectious osteoporosis. Int J Biol Macromol 320: 145769, 2025.
30. Li P, Dai J, Li Y, Alexander D, Čapek J, Geis-Gerstorfer J, Wan G, Han J, Yu Z and Li A: Zinc based biodegradable metals for bone repair and regeneration: Bioactivity and molecular mechanisms. Mater Today Bio 25: 100932, 2024.
31. Pietrangelo A: Iron and the Liver. Liver Int 36 (Suppl 1): S116-S123, 2016.
32. Wu Z, Zhu Y, Liu W, Balasubramanian B, Xu X, Yao J and Lei X: Ferroptosis in liver disease: Natural active compounds and therapeutic implications. Antioxidants (Basel) 13: 352, 2024.
33. Karadeniz F, Oh JH, Lee JI, Seo Y and Kong CS: 3,5-dicaffeoyl-epi-quinic acid from *Atriplex gmelinii* enhances the osteoblast differentiation of bone marrow-derived human mesenchymal stromal cells via WnT/BMP signaling and suppresses adipocyte differentiation via AMPK activation. Phytomedicine 71: 153225, 2020.
34. Bauer NB, Khassawna TE, Goldmann F, Stirn M, Ledieu D, Schlewitz G, Govindarajan P, Zahner D, Weisweiler D, Schliefke N, *et al*: Characterization of bone turnover and energy metabolism in a rat model of primary and secondary osteoporosis. Exp Toxicol Pathol 67: 287-296, 2015.
35. Komori T: Whole aspect of Runx2 functions in skeletal development. Int J Mol Sci 23: 5776, 2022.
36. Fakhry M, Hamade E, Badran B, Buchet R and Magne D: Molecular mechanisms of mesenchymal stem cell differentiation towards osteoblasts. World J Stem Cells 5: 136-148, 2013.
37. Lee B, Thirunavukkarasu K, Zhou L, Pastore L, Baldini A, Hecht J, Geoffroy V, Ducy P and Karsenty G: Missense mutations abolishing DNA binding of the osteoblast-specific transcription factor OSF2/CBFA1 in cleidocranial dysplasia. Nat Genet 16: 307-310, 1997.
38. Ozaki Y, Koide M, Furuya Y, Ninomiya T, Yasuda H, Nakamura M, Kobayashi Y, Takahashi N, Yoshinari N and Udagawa N: Treatment of OPG-deficient mice with WP9QY, a Rankl-binding peptide, recovers alveolar bone loss by suppressing osteoclastogenesis and enhancing osteoblastogenesis. PLoS One 12: e0184904, 2017.
39. Zhu R, Wang Z, Xu Y, Wan H, Zhang X, Song M, Yang H, Chai Y and Yu B: High-fat diet increases bone loss by inducing ferroptosis in osteoblasts. Stem Cells Int 2022: 9359429, 2022.
40. Yang Y, Lin Y, Wang M, Yuan K, Wang Q, Mu P, Du J, Yu Z, Yang S, Huang K, *et al:* Targeting ferroptosis suppresses osteocyte glucolipotoxicity and alleviates diabetic osteoporosis. Bone Res 10: 26, 2022.
41. Wang X, Ma H, Sun J, Zheng T, Zhao P, Li H and Yang M: Mitochondrial ferritin deficiency promotes osteoblastic ferroptosis via mitophagy in type 2 diabetic osteoporosis. Biol Trace Elem Res 200: 298-307, 2022.
42. Zimmermann MB and Hurrell RF: Nutritional iron deficiency. Lancet 370: 511-520, 2007.
43. Clark SF: Iron deficiency anemia. Nutr Clin Pract 23: 128-141, 2008.
44. Shen GS, Yang Q, Jian JL, Zhao GY, Liu LL, Wang X, Zhang W, Huang X and Xu YJ: Hepcidin1 knockout mice display defects in bone microarchitecture and changes of bone formation markers. Calcif Tissue Int 94: 632-639, 2014.
45. Lu H, Lian L, Shi D, Zhao H and Dai Y: Hepcidin promotes osteogenic differentiation through the bone morphogenetic protein 2/small mothers against decapentaplegic and mitogen-activated protein kinase/P38 signaling pathways in mesenchymal stem cells. Mol Med Rep 11: 143-150, 2015.
46. Fang Y, Chen X, Tan Q, Zhou H, Xu J and Gu Q: Inhibiting ferroptosis through disrupting the NCOA4-FTH1 interaction: A new mechanism of action. ACS Cent Sci 7: 980-989, 2021.
47. Liu P, Zhang Z, Cai Y, Li Z, Zhou Q and Chen Q: Ferroptosis: Mechanisms and role in diabetes mellitus and its complications. Ageing Res Rev 94: 102201, 2024.

48. Le Y, Liu Q, Yang Y, Stanford D, Freeman WM and Ding XQ: The emerging role of nuclear receptor coactivator 4 in health and disease: A novel bridge between iron metabolism and Immunity. Cell Death Discov 10: 312, 2024.
49. Zhang Z, Ji C, Wang YN, Liu S, Wang M, Xu X and Zhang D: Maresin1 Suppresses High-Glucose-induced ferroptosis in osteoblasts via NRF2 Activation in type 2 diabetic osteoporosis. Cells 11: 2560, 2022.
50. Kuang F, Liu J, Xie Y, Tang D and Kang R: MGST1 is a redox-sensitive repressor of ferroptosis in pancreatic cancer cells. Cell Chem Biol 28: 765-775.e5, 2021.
51. Fan Z, Wirth AK, Chen D, Wruck CJ, Rauh M, Buchfelder M and Savaskan N: Nrf2-Keap1 pathway promotes cell proliferation and diminishes ferroptosis. Oncogenesis 6: e371, 2017.
52. Rojo de la Vega M, Chapman E and Zhang DD: NRF2 and the hallmarks of cancer. Cancer Cell 34: 21-43, 2018.
53. Chen Y, Jiang Z and Li X: New insights into crosstalk between Nrf2 pathway and ferroptosis in lung disease. Cell Death Dis 15: 841, 2024.
54. Živanović N, Lesjak M, Simin N and Srai SKS: Beyond mortality: Exploring the influence of plant phenolics on modulating Ferroptosis-A systematic review. Antioxidants (Basel) 13: 334, 2024.
55. Zhou HM, Liu Y, Shi F, Qiu HW, Li L, Shu QP, Liu YY, Wang BQ, Gao M, Du RL, *et al*: CLK2 Regulates the KEAP1/NRF2 and p53 pathways to suppress ferroptosis in colorectal cancer. Cancer Res 85: 4734-4750, 2025.
56. Duan CH and Jiang LL: High-dose Yin Chen combined with Western medicine for liver protection in treating acute icteric hepatitis. Youjiang Med J: 383, 2001.
57. Chen GE and Huang XD: Large dose of Yin Chen in the treatment of 84 cases of acute infectious icteric hepatitis: A therapeutic effect observation. Jilin J Tradit Chin Med: 19, 1984.